INTERNATIONAL JOURNAL FOR NUMERICAL METHODS IN FLUIDS
Int. J. Numer. Meth. Fluids 2011; **66**:939–962
Published online 22 February 2010 in Wiley Online Library (wileyonlinelibrary.com). DOI: 10.1002/fld.2288

Implementing a high-order accurate implicit operator scheme for solving steady incompressible viscous flows using artificial compressibility method

Kazem Hejranfar*, †, ‡ and Ali Khajeh-Saeed

Aerospace Engineering Department, Sharif University of Technology, Tehran, Iran

SUMMARY

This paper uses a fourth-order compact finite-difference scheme for solving steady incompressible flows. The high-order compact method applied is an alternating direction implicit operator scheme, which has been used by Ekaterinaris for computing two-dimensional compressible flows. Herein, this numerical scheme is efficiently implemented to solve the incompressible Navier–Stokes equations in the primitive variables formulation using the artificial compressibility method. For space discretizing the convective fluxes, fourth-order centered spatial accuracy of the implicit operators is efficiently obtained by performing compact space differentiation in which the method uses block-tridiagonal matrix inversions. To stabilize the numerical solution, numerical dissipation terms and/or filters are used. In this study, the high-order compact implicit operator scheme is also extended for computing three-dimensional incompressible flows. The accuracy and efficiency of this high-order compact method are demonstrated for different incompressible flow problems. A sensitivity study is also conducted to evaluate the effects of grid resolution and pseudocompressibility parameter on accuracy and convergence rate of the solution. The effects of filtering and numerical dissipation on the solution are also investigated. Test cases considered herein for validating the results are incompressible flows in a 2-D backward facing step, a 2-D cavity and a 3-D cavity at different flow conditions. Results obtained for these cases are in good agreement with the available numerical and experimental results. The study shows that the scheme is robust, efficient and accurate for solving incompressible flow problems. Copyright © 2010 John Wiley & Sons, Ltd.

Received 5 June 2008; Revised 10 December 2009; Accepted 13 December 2009

KEY WORDS: incompressible flows; artificial compressibility method; high-order accurate implicit operator scheme; numerical dissipation term

1. INTRODUCTION

The Navier–Stokes equations which are used to compute incompressible flow problems are highly nonlinear and difficult to solve, especially when high-order accuracy solutions are needed. High-order accurate numerical methods used to solve the incompressible Navier–Stokes equations allow studies of more practical problems where grid refinements are required to accurately represent flow physics.

The main difficulty in solving the incompressible Navier–Stokes equations lies in satisfying the divergence-free velocity condition. The Navier–Stokes equations may be rearranged in the

*Correspondence to: Kazem Hejranfar, Aerospace Engineering Department, Sharif University of Technology, Tehran, Iran.
†E-mail: khejran@sharif.edu
‡Associate Professor.

Contract/grant sponsor: Sharif University of Technology

stream function-vorticity formulation [1, 2] or the artificial compressibility approach [3]. Although the stream function–vorticity method is an efficient scheme for computing two-dimensional incompressible flow problems, the extension of this method to 3-D flows is quite inappropriate. The artificial compressibility method introduced by Chorin [3] provides a mechanism to advance the flowfield in pseudo-time to satisfy the divergence-free velocity condition in a manner that the mass and momentum equations are conserved when a steady-state in pseudo-time is obtained. In addition, the artificial compressibility method changes the nature of the governing equations from the mixed elliptic/parabolic into a system of hyperbolic or parabolic equations in artificial time that can be solved by efficient time-marching schemes. Moreover, the implementation of the artificial compressibility method to solve 3-D incompressible flow problems is straightforward.

The main objective of the present work is to implement a fourth-order compact implicit operator scheme to the incompressible Navier–Stokes equations. Compact formulations, compared with the traditional finite-difference schemes of the same order of accuracy, are shown to achieve more accurate solutions with benefit of having good resolution properties without exceedingly increasing the computational stencil size. In addition, they are more stable and robust in terms of geometry and boundary conditions than spectral schemes. Up to now, many efforts for developing efficient and accurate numerical methods for computing incompressible flows have been made (see References [4–11]). Efficient highly accurate finite-difference and finite-volume methods on staggered grids have been performed for the numerical solution of the incompressible flow equations [4, 5]. For steady-state Navier–Stokes equations, a family of compact schemes [6–8] has been demonstrated to be computationally efficient and stable and yield accurate numerical results. Ekaterinaris [9] has used a high-order accurate numerical scheme for solving incompressible flow problems using the artificial compressibility method. For time-dependent problems, he has used an implicit dual-time stepping procedure which is more appropriate for time accurate simulations. The linearization is for pseudo-time and therefore, the method needs an iterative procedure for the solution to be obtained. Liu [10] solved the unsteady incompressible Navier–Stokes equations using high-order accurate methods. High-order accurate finite element methods based on high-order expansions of the discrete solution have also been performed [11].

The high-order compact method used herein is an alternating direction implicit operator scheme which has been proposed by Ekaterinaris [12, 13] for computing two-dimensional compressible flows. In the present study, this numerical scheme is efficiently implemented to solve the incompressible Navier–Stokes equations in the primitive variables formulation using the artificial compressibility method [14, 15]. For space discretizing the convective fluxes, fourth-order centered spatial accuracy of the implicit operators is efficiently obtained by performing compact space differentiation in which the method uses block-tridiagonal matrix inversions. In this study, the high-order compact implicit operator scheme is also extended for computing three-dimensional incompressible flows. High-order spectral-type low-pass compact filters are used to regularize the numerical solution and eliminate spurious modes due to unresolved scales, non-linearities and inaccuracies in applying boundary conditions. In addition, the sixth-order numerical dissipation terms are used to stabilize the numerical solution and the effects of filtering and numerical dissipation on the solution are also investigated. The present computations are performed for different incompressible flow problems to demonstrate the accuracy and efficiency of the high-order accurate numerical method applied. Test cases studied herein for verifying the present solutions are incompressible flows in a 2-D backward facing step, a 2-D cavity and a 3-D cavity at different flow conditions. The present computations for these cases are compared with the available numerical and experimental results. The study indicates the scheme implemented is robust, efficient and accurate for computing incompressible flow problems.

The organization of the paper is as follows. Section 2 describes the governing equation and the artificial compressibility approach. Section 3 introduces the high-order compact implicit operator scheme implemented to solve the incompressible Navier–Stokes equations. The numerical dissipation terms used and the filtering scheme are given in Section 4. The boundary conditions and the properties of the numerical scheme used are described in Sections 5 and 6 respectively.

DOI: 10.1002/fld

Finally, Section 7 is devoted to present the numerical results for the two- and three-dimensional incompressible benchmark problems to validate the results obtained.

2. GOVERNING EQUATIONS

The main goal of this paper is to implement a high-order compact implicit operator scheme to the incompressible Navier–Stokes equations with the artificial compressibility approach. The primary problem with solutions of the incompressible Navier–Stokes equations is the difficulty of coupling changes in the velocity field with changes in the pressure field while satisfying the continuity equation. The artificial compressibility or pseudocompressibility method is an efficient approach to overcome this difficulty. This method is also straightforward for solving three-dimensional incompressible flow problems. The artificial compressibility method was initially introduced by Chorin [3] for the solution of steady-state incompressible flows, and then it was extended to time-accurate numerical solutions of incompressible flows [9, 16]. The artificial compressibility formulation can be used for the solution of incompressible flows by adding a pseudo-time derivative of density to the continuity equation as follows:

$$\frac{\partial \tilde{\rho}}{\partial t}+\frac{\partial u}{\partial x}+\frac{\partial v}{\partial y}+\frac{\partial w}{\partial z}=0 \tag{1}$$

Then, the artificial density may be replaced by the pressure term by the following state equation:

$$p=\beta\tilde{\rho} \tag{2}$$

In this equation, β is the artificial compressibility or pseudocompressibility coefficient and $\beta^{1/2}$ is the artificial sound speed. Then, the continuity equation may be written as

$$\frac{1}{\beta}\frac{\partial p}{\partial t}+\frac{\partial u}{\partial x}+\frac{\partial v}{\partial y}+\frac{\partial w}{\partial z}=0 \tag{3}$$

The added term directly couples the pressure field with the velocity field and allows the governing equations to march in the artificial time until a divergence-free velocity field is obtained at the steady-state condition. The parameter β usually takes a value between 1 and 10, or may be chosen variable [17, 18]. It should be noted that the best value of the artificial compressibility parameter β depends on the characteristic velocity in the flowfield, and therefore, the value of the optimum β changes when the characteristic velocity varies.

The three-dimensional incompressible Navier–Stokes equations using the artificial compressibility method can be written in dimensionless and conservative form in Cartesian coordinates as

$$\frac{\partial Q}{\partial t}+\frac{\partial E}{\partial x}+\frac{\partial F}{\partial y}+\frac{\partial G}{\partial z}=\frac{1}{Re}[N]\nabla^2 Q \tag{4}$$

where $Q=(p,u,v,w)^T$ is the solution vector and E, F and G are the inviscid flux vectors as follows

$$E=\begin{pmatrix}\beta u\\ u^2+p\\ uv\\ uw\end{pmatrix},\quad F=\begin{pmatrix}\beta v\\ uv\\ v^2+p\\ vw\end{pmatrix},\quad G=\begin{pmatrix}\beta w\\ uw\\ vw\\ w^2+p\end{pmatrix},\quad N==\begin{pmatrix}0&0&0&0\\0&1&0&0\\0&0&1&0\\0&0&0&1\end{pmatrix} \tag{5}$$

In the above equations, p is the pressure, (u,v,w) are the Cartesian velocity components, $Re=u_{\mathrm{ref}}L_{\mathrm{ref}}/v$ denotes the Reynolds number based on a characteristic length L_{ref}, and a characteristic velocity u_{ref}, and v is the kinematic viscosity.

DOI: 10.1002/fld

3. HIGH-ORDER IMPLICIT DISCRITIZATION

In this section, the numerical procedure based on a fourth-order compact finite-difference scheme for solving the steady incompressible flows is described [14, 15]. The high-order compact method used is an alternating direction implicit operator scheme, which has been used by Ekaterinaris [12, 13] for computing two-dimensional compressible flows. Herein, this numerical scheme is efficiently implemented to solve both the two- and three-dimensional incompressible Navier–Stokes equations in the primitive variables formulation using the artificial compressibility method.

The governing equations considered are a nonlinear system of equations. When implicit formulations are utilized, a linearization procedure must be introduced. Using the Taylor series expansion for each flux vector, i.e. E, one can obtain

$$E^{n+1} = E^n + \left(\frac{\partial E}{\partial Q}\right)^n \Delta Q + O(\Delta t^2) \tag{6}$$

where $\Delta Q = Q^{n+1} - Q^n$ and terms such as $\partial E/\partial Q$, $\partial F/\partial Q$ and $\partial G/\partial Q$ are known as flux Jacobian matrices, denoted by A, B and C respectively, as follows

$$A = \begin{pmatrix} 0 & \beta & 0 & 0 \\ 1 & 2u & 0 & 0 \\ 0 & v & u & 0 \\ 0 & w & 0 & u \end{pmatrix}, \quad B = \begin{pmatrix} 0 & 0 & \beta & 0 \\ 0 & v & u & 0 \\ 1 & 0 & 2v & 0 \\ 0 & 0 & w & v \end{pmatrix}, \quad C = \begin{pmatrix} 0 & 0 & 0 & \beta \\ 0 & w & 0 & u \\ 0 & 0 & w & v \\ 1 & 0 & 0 & 2w \end{pmatrix} \tag{7}$$

After the linearization of all flux vectors, the following operator form of equations can be obtained

$$\left[I + \Delta t\left(\frac{\partial A}{\partial x} - \frac{N}{Re}\frac{\partial^2}{\partial x^2}\right)\right]\left[I + \Delta t\left(\frac{\partial B}{\partial y} - \frac{N}{Re}\frac{\partial^2}{\partial y^2}\right)\right]\left[I + \Delta t\left(\frac{\partial C}{\partial z} - \frac{N}{Re}\frac{\partial^2}{\partial z^2}\right)\right]\Delta Q = RHS$$

$$RHS = \Delta t\left[-\frac{\partial E}{\partial x} - \frac{\partial F}{\partial y} - \frac{\partial G}{\partial z} + \frac{N}{Re}\left(\frac{\partial^2 Q}{\partial x^2} + \frac{\partial^2 Q}{\partial y^2} + \frac{\partial^2 Q}{\partial z^2}\right)\right] \tag{8}$$

For two- and three-dimensional problems, the above implicit formulation results in a block-penta and heptadiagonal system of equations, respectively. The solution of such systems needs a relatively more computational effort than a block-tridiagonal solver. To overcome this difficulty, an implicit approximate factorization scheme for each time step can be used

$$\left[I + \Delta t\left(\frac{\partial A}{\partial x} - \frac{N}{Re}\frac{\partial^2}{\partial x^2}\right)\right]\Delta Q^{**} = \mathrm{RHS} \tag{9}$$

$$\left[I + \Delta t\left(\frac{\partial B}{\partial y} - \frac{N}{Re}\frac{\partial^2}{\partial y^2}\right)\right]\Delta Q^{*} = \Delta Q^{**} \tag{10}$$

$$\left[I + \Delta t\left(\frac{\partial C}{\partial z} - \frac{N}{Re}\frac{\partial^2}{\partial z^2}\right)\right]\Delta Q = \Delta Q^{*} \tag{11}$$

in which for the second-order accuracy in space, the solution requires a block-tridiagonal matrix inversion in the x, y and z directions to calculate incremental solution vector ΔQ. The above formulation for computing incompressible flows is known as the Beam–Warming method [19], which originally has been developed for solving compressible flows.

DOI: 10.1002/fld

For steady solutions, one can assume the second derivatives of flow variables describing the viscous terms in the left-hand side of Equations (9)–(11) to be omitted, i.e.

$$\frac{\partial^2}{\partial x^2}=\frac{\partial^2}{\partial y^2}=\frac{\partial^2}{\partial z^2}=0 \tag{12}$$

Having this assumption, Equations ((9)–(11)) can be rewritten as follows:

$$\frac{\partial}{\partial x}(A\Delta Q^{**})=\frac{1}{\Delta t}(\mathrm{RHS}-\Delta Q^{**}) \tag{13}$$

$$\frac{\partial}{\partial y}(B\Delta Q^{*})=\frac{1}{\Delta t}(\Delta Q^{**}-\Delta Q^{*}) \tag{14}$$

$$\frac{\partial}{\partial z}(C\Delta Q)=\frac{1}{\Delta t}(\Delta Q^{*}-\Delta Q) \tag{15}$$

The 1st derivative of the function f (denoted by f') may be computed with the fourth-order compact scheme as [20, 21]

$$f'_{i-1}+4f'_i+f'_{i+1}=\frac{3}{h}(f_{i+1}-f_{i-1})+O(h^4) \tag{16}$$

Now by substituting Equations (13)–(15) into Equation (16) and rearranging all terms, the following relations for the fourth-order implicit operator algorithm can be obtained

$$\begin{aligned}&\left(I-3\frac{\Delta t}{\Delta x}A_{i-1,j,k}\right)\Delta Q^{**}_{i-1,j,k}+4\Delta Q^{**}_{i,j,k}+\left(I+3\frac{\Delta t}{\Delta x}A_{i+1,j,k}\right)\Delta Q^{**}_{i+1,j,k}\\&\quad=\mathrm{RHS}_{i-1,j,k}+4\mathrm{RHS}_{i,j,k}+\mathrm{RHS}_{i+1,j,k}\end{aligned} \tag{17}$$

$$\begin{aligned}&\left(I-3\frac{\Delta t}{\Delta y}B_{i,j-1,k}\right)\Delta Q^{*}_{i,j-1,k}+4\Delta Q^{*}_{i,j,k}+\left(I+3\frac{\Delta t}{\Delta y}B_{i,j+1,k}\right)\Delta Q^{*}_{i,j+1,k}\\&\quad=\Delta Q^{**}_{i,j-1,k}+4\Delta Q^{**}_{i,j,k}+\Delta Q^{**}_{i,j+1,k}\end{aligned} \tag{18}$$

$$\begin{aligned}&\left(I-3\frac{\Delta t}{\Delta z}C_{i,j,k-1}\right)\Delta Q_{i,j,k-1}+4\Delta Q_{i,j,k}+\left(I+3\frac{\Delta t}{\Delta z}C_{i,j,k+1}\right)\Delta Q_{i,j,k+1}\\&\quad=\Delta Q^{*}_{i,j,k-1}+4\Delta Q^{*}_{i,j,k}+\Delta Q^{*}_{i,j,k+1}\end{aligned} \tag{19}$$

Note that the spatial derivatives in the right-hand side of Equation (17) are computed with the fourth-order compact scheme. The preceding system of Equations (17)–(19) along with appropriate boundary conditions form a block-tridiagonal system of equations with a block size of 4×4 in the I, J and K sweeps to obtain $\Delta Q_{i,j,k}$ and then calculate the solution vector $Q^{n+1}_{i,j,k}$ at the new time step as

$$Q^{n+1}_{i,j,k}=Q^{n}_{i,j,k}+\Delta Q_{i,j,k} \tag{20}$$

The high-order compact implicit operator scheme used herein requires only a moderate increase in computational effort than the second-order central implicit method because it needs a slightly larger operation count to construct the coefficient matrices.

DOI: 10.1002/fld

4. NUMERICAL DISSIPATION TERMS AND FILTERING SCHEME

The centered compact finite-difference methods are nondissipative and are therefore sensitive to numerical instabilities due to the growth of high-frequency modes. These difficulties originate usually from grid nonuniformity, boundary conditions and also nonlinear flow features [22]. These difficulties can be overcome either by using a numerical dissipation term or by applying a spatial filtering to the solution vector.

High-order dissipation terms are added to the compact scheme in order to damp high-frequency oscillations associated with the central differencing of derivatives. Herein, the sixth-order numerical dissipation terms of the form

$$D_e = \frac{\varepsilon_e}{\Delta t}[(\Delta x)^6 Q_{xxxxxx} + (\Delta y)^6 Q_{yyyyyy} + (\Delta z)^6 Q_{zzzzzz}] \tag{21}$$

are added to the right-hand side of Equation (17) to stabilize the numerical instability of the compact method. The stability bound for the numerical dissipation coefficient $\varepsilon_e = \varepsilon_e^{(6)}$ for the two- and three-dimensional formulations is obtained from the stability analysis of the numerical method as $0 \leqslant \varepsilon_e^{(6)} \leqslant 1/64$ and $0 \leqslant \varepsilon_e^{(6)} \leqslant 1/96$, respectively (see Appendix A). Note that the second-order central implicit (Beam–Warming) scheme also requires high-order dissipation terms. Therefore, fourth-order explicit dissipation terms must be added to the right-hand side of Equation (9) to stabilize the Beam–Warming method. The stability bound for the fourth-order dissipation coefficient $\varepsilon_e^{(4)}$ for two- and three-dimensional formulations is $0 \leqslant \varepsilon_e^{(4)} \leqslant 1/8$ and $0 \leqslant \varepsilon_e^{(4)} \leqslant 1/16$, respectively [19].

In this study, a high-order implicit filtering technique [23, 24] is also used. The implicit filters obtain the filtered variables $\hat{\psi}$ from the unfiltered values ψ by solving the following tridiagonal system of equations

$$a_f \hat{\psi}_{i-1} + \hat{\psi}_i + a_f \hat{\psi}_{i+1} = \sum_{n=0}^{n-N} \frac{a_{n,i}}{2}(\psi_{i+n} + \psi_{i-n}) \tag{22}$$

With proper choice of coefficients, this relation provides a $2N$th-order accurate formula on a $2N+1$ point stencil [20–23]. The $N+1$ coefficients, $a_0, a_1, a_2, \ldots, a_{N-1}, a_N$, are derived in terms of a_f with Taylor and Fourier-series analyses (see Tables I and II). The parameter a_f satisfies the inequality $-0.5 < a_f < 0.5$, in which a higher value of a_f represents a less dissipative filter. The filter is typically selected to be at least two orders of accuracy higher than the difference scheme. In the present study, both sixth- and eight-order filters are used for the calculations (see Table I).

Special relations are needed at near boundary points due to the relatively large stencil of the filter. The flow variables at the end points, $i = 1, I\,\max$, $j = 1, J\,\max$ and $k = 1, K\,\max$ are not filtered. At other near boundary points, where Equation (22) cannot be used, two approaches are appropriate. In the first method, proposed in Reference [23], the order of accuracy is reduced upon

Table I. Filter coefficients at interior points.

Order	a_0	a_1	a_2	a_3	a_4
$F(O(\Delta x^6))$	$\frac{11+10\alpha_f}{16}$	$\frac{15+34\alpha_f}{32}$	$\frac{-3+6\alpha_f}{16}$	$\frac{1-2\alpha_f}{32}$	0
$F(O(\Delta x^8))$	$\frac{93+70\alpha_f}{128}$	$\frac{7+18\alpha_f}{16}$	$\frac{-7+14\alpha_f}{32}$	$\frac{1-2\alpha_f}{16}$	$\frac{-1+2\alpha_f}{128}$

Table II. Sixth-order filter coefficients at points 2 and 3.

Order	a_1	a_2	a_3	a_4	α_5	α_6	α_7
$F_2(O(\Delta x^6))$	$\frac{1+62\alpha_f}{64}$	$\frac{29+6\alpha_f}{32}$	$\frac{15+24\alpha_f}{64}$	$\frac{-5+10\alpha_f}{16}$	$\frac{15-30\alpha_f}{64}$	$\frac{-3+6\alpha_f}{32}$	$\frac{1-2\alpha_f}{64}$
$F_3(O(\Delta x^6))$	$\frac{-1+2\alpha_f}{64}$	$\frac{3+26\alpha_f}{32}$	$\frac{49+30\alpha_f}{64}$	$\frac{5+6\alpha_f}{16}$	$\frac{-15+30\alpha_f}{64}$	$\frac{3-6\alpha_f}{32}$	$\frac{-1+2\alpha_f}{64}$

DOI: 10.1002/fld

approaching the boundary to a level that a centered scheme is available. This approach is suitable for problems where the mesh is highly refined near the boundary. The second method, introduced in Reference [24] employs higher order one-sided formulas, which can retain the tridiagonal form of the scheme. In this study, the second approach is used due to the uniform mesh considered for all cases. At a near boundary point i, a filter formula is given by

$$a_f\hat{\psi}_{i-1}+\hat{\psi}_i+a_f\hat{\psi}_{i+1}=\sum_{n=1}^{7}a_{n,i}\psi_n \quad i\in(2,3) \tag{23}$$

$$a_f\hat{\psi}_{i-1}+\hat{\psi}_i+a_f\hat{\psi}_{i+1}=\sum_{n=1}^{7}a_{I\max-n,i}\psi_{I\max-n} \quad i\in(I\max-2, I\max-1) \tag{24}$$

This boundary filter retains the tridiagonal form of the filter scheme, and a_f remains as the only free parameter. Table II gives the coefficients for the higher-order one-sided left-boundary filter formulas used in the present computations at points 2 and 3. The right-boundary formulas are obtained by noting that $a_{I\max-n,i}=a_{n+1,I\max-n+1}$ for $i\in(I\max-2, I\max-1)$. A complete list of the boundary filter coefficients can be found in References [24, 25]. In the present computations, the filter is applied to the primitive variable and sequentially in all coordinate directions. Note that the solution is filtered once after each time step of the implicit algorithm. In the present study, for boundary points a sixth-order filter is used for all calculations (see Table II).

The effects of numerical dissipation value and the filtering coefficient on the accuracy and the performance of the numerical method are discussed in the numerical results section.

5. BOUNDARY CONDITIONS

The fourth-order compact operator implicit scheme applied requires appropriate boundary conditions. Equations (17)–(19) are applied in the computational domain for the grid points $i=2,\ldots,I\max-1$, $j=2,\ldots,J\max-1$ and $k=2,\ldots,K\max-1$, because in the right-hand side of Equation (17), the residual term RHS is calculated with a three-point stencil. For the i sweep, the terms $\mathrm{RHS}_{1,j,k}$ and $\mathrm{RHS}_{I\max,j,k}$ in Equation (17) must be computed for the inversion. These terms at boundary points can be calculated with appropriate one-sided compact relations. In the present calculations, the residual term at boundary points is computed by the relations developed by Carpenter *et al.* [26]. For example, for evaluating $\partial u/\partial x$, we use the following the third-order one-sided boundary condition formulas

$$u'_1+2u'_2=\frac{1}{2\Delta x}(-5u_1+4u_2+u_3)+O(\Delta x^3) \tag{25}$$

$$u'_{I\max}+2u'_{I\max-1}=\frac{1}{2\Delta x}(5u_{I\max}-4u_{I\max-1}-u_{I\max-2})+O(\Delta x^3) \tag{26}$$

These relations together with the fourth-order compact formula (16) are used to compute $\partial u/\partial x$ implicitly for $i=i,\ldots,I\max$ for all j and k. Other spatial derivatives needed for calculating the residual term RHS are computed in the same manner. The solution can also be obtained by using explicit updating the computational domain boundaries by setting the residual term $\mathrm{RHS}_{i,j,k}$ to be zero at the edges of the computational domain [12].

To form the block-tridiagonal system of equations during the i sweep, appropriate boundary conditions are to be used for $\Delta Q^{**}_{i,j,k}$ at $i=1$ and $i=I\max$. For example, for the inlet boundary $i=1$, by setting the velocity to be constant, then we have $\Delta u^{**}_{1,j,k}=\Delta v^{**}_{1,j,k}=\Delta w^{**}_{1,j,k}=0$ and by assuming a zero pressure gradient approximation ($\partial p/\partial x=0$) one can employ the second-order one-sided difference approximation to obtain $\Delta p^{**}_{1,j,k}=(4\Delta p^{**}_{2,j,k}-\Delta p^{**}_{3,j,k})/3$. For the outlet boundary $i=I\max$, using an extrapolation to calculate the velocity by setting $\partial u/\partial x=0$ one can obtain $\Delta u^{**}_{I\max,j,k}=(4\Delta u^{**}_{I\max-1,j,k}-\Delta u^{**}_{I\max-2,j,k})/3$ and by assuming a constant value for the pressure we have $\Delta p^{**}_{I\max,j,k}=0$. Now, $\Delta Q^{**}_{i,j,k}$ at the inlet and outlet boundaries in Equation (17)

DOI: 10.1002/fld

can be expressed in terms of $\Delta Q^{**}_{i,j,k}$ at the neighboring points of each boundary and therefore, the block-tridiagonal system (17) can be solved to obtain $\Delta Q^{**}_{i,j,k}$ at the desired grid points. Note that the use of a third-order one-sided difference formula for the boundary condition of Neumann type wipes out the block tridiagonal nature of the matrices involved. However, the desirable block-tridiagonality can be restored by using a simple algebraic manipulation.

It should be noted that all boundary conditions used are either of Dirichlet or of Neumann type (see Numerical Results section) and the treatment described above can also be applied for the implicit j and k sweeps. Herein, after each time step, the accuracy of the flow variables computed at the boundaries of Neumann type is improved by applying a high-order finite-difference formula. For example, for updating the pressure at the inlet, using the fourth-order finite-difference approximation for $\partial p/\partial x=0$, one can obtain $p_1=(48p_2-36p_3+16p_4-3p_5)/25$. The present study indicates that the procedure used for implementing the boundary conditions is stable for the implicit compact solution of the incompressible flows.

6. STABILITY AND CONVERGENCE

The properties of the high-order compact implicit operator scheme used herein have been described in detail by Ekaterinaris [12]. He used this scheme for computing two-dimensional compressible flows, and in the present work, this numerical scheme is efficiently implemented for solving two- and three-dimensional incompressible flows with the artificial compressibility method. Ekaterinaris performed an eigenspectrum analysis of the second- and fourth-order central and fourth-order compact schemes for the simple advection equation, $u_t+au_x=0$ (where a is a constant wave speed) and their stability discussed. This equation is a good model for describing and studying the properties of numerical approximations of hyperbolic systems [27]. The numerical stability analysis has shown that the fourth-order accurate implicit operator scheme used is unconditionally stable for the linear advection equation and faster convergence is achieved with the fourth-order compact implicit tridiagonal scheme compared to the second-order implicit tridiagonal or the fourth-order explicit pentadiagonal schemes [12]. It was also shown that the fourth-order compact method is unconditionally stable for the linear two-dimensional wave equation [13]. Herein, the stability analysis for the three-dimensional wave equation, $u_t+a(u_x+u_y+u_z)=0$, is performed with the sixth-order numerical dissipation term added to the differenced equation and the stability band is obtained (see Appendix A). The present computations indicate that the high-order compact implicit operator scheme used is robust, efficient and accurate for solving two- and three-dimensional incompressible flow problems.

7. NUMERICAL RESULTS

The accuracy and efficiency of the high-order accurate implicit operator scheme implemented to the incompressible Navier–Stokes equations are demonstrated for different incompressible flow problems. Three benchmark cases are considered for verifying the computations: a 2-D backward facing step, a 2-D cavity and a 3-D cavity at different flow conditions. Results obtained for these cases are compared with the available numerical results and experimental data. A sensitivity study is also performed to evaluate the effects of grid resolution and pseudocompressibility parameter on accuracy and convergence rate of the solution. The effects of filtering and numerical dissipation on the solution are also studied.

7.1. Flow over a backward facing step

The flow past a backward facing step is a good test case to examine the accuracy and performance of a numerical method implemented. Figure 1 shows the geometry of this test case and the defined important flow parameters. Although the geometry is simple, it contains complex flow features associated with separation and reattachment. The main difficulty in applying numerical schemes

DOI: 10.1002/fld

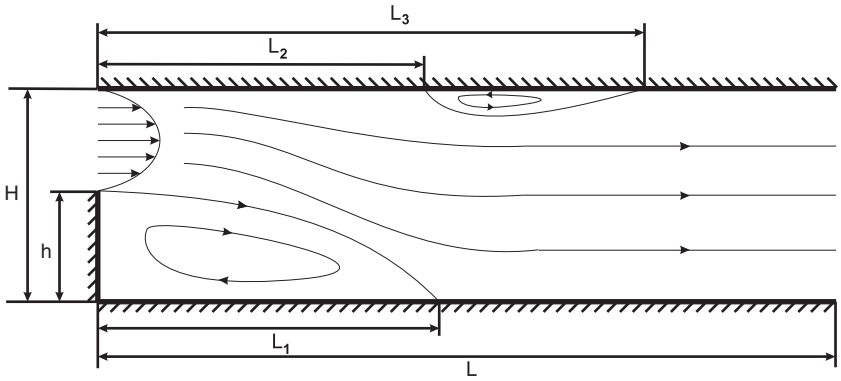

Figure 1. Geometry of backward facing step including defined important flow parameters.

to this test case is the highly dependence of the recirculation regions with respect to grid size and grid resolution, and for an accurate solution one should use the numerical methods with high-order accuracy. Herein, the fourth-order compact implicit operator scheme is used for this test case to accurately compute the flowfield characteristics.

The flow over the backward facing step involves different boundary conditions including noslip, inflow and outflow conditions. At the inlet, the velocity is given by a parabolic condition, $u(y)=6\bar{u}(H-y)(y-h)/(H-h)^2$ and an extrapolation is used for computing the pressure by setting $\partial p/\partial x=0$. The noslip conditions for the velocity components are imposed for both the upper and lower walls and an extrapolation is used for calculating the pressure by setting $\partial p/\partial y=0$. At the outlet, an extrapolation is used to calculate the velocity and the pressure is set to be a fixed value, which may be the initial condition for the pressure in the flowfield. The Reynolds number $Re=\bar{u}H/\nu$ is defined based on the mean inflow velocity $\bar{u}$, the channel height H, and the kinematics viscosity ν. In order to achieve the fully developed condition at the outflow boundary, the channel length is considered to be 50 and 70 step heights for $200\leqslant Re<1000$ and $Re\geqslant 1000$, respectively.

At first, to validate the results and obtain the order of the accuracy of the numerical method implemented, the flow in a two-dimensional simple channel ($h=0$ in Figure 1) is computed. For this case, the analytical solution is available and the fully developed u-velocity profile is given by $u(y)=6\bar{u}(H-y)y/H^2$. This profile is prescribed at the inlet of the channel while the outflow boundary consists of zero-normal velocity derivatives. The channel length is considered to be $L/H=2$ and the results are presented for $Re=80$. Note that the steady-state solution for the simple channel for the fully developed condition does not depend on Reynolds number Re. Figure 2 compares the u-velocity profile computed at the outlet for the different grid sizes with the exact solution, which exhibits excellent agreement. The order of accuracy of the solution for this case is about 3.83 that verifies the fourth-order accuracy of the numerical method employed (see Table III). The error is calculated based on the L_2 norm of divergence of the velocity vector at the outlet for the four meshes compared with the exact solution. Note the exact value of the divergence of the velocity is zero everywhere.

Now, we examine the accuracy and performance of the compact method employed in computing the flow past the backward facing step ($h=H/2$ in Figure 1). For the backward facing step problem, both the numerical and experimental results are available. Armaly *et al.* [28] have presented extensive experimental data for Reynolds numbers up to 800 and many computational studies also appear in the literature [29–39]. The experimental results by Armaly *et al.* indicate that a secondary recirculating flow region develops at the upper wall for Reynolds numbers higher than 400. Their study shows that the three-dimensional effects occur for $Re\geqslant 400$ and the experimental data and the theoretical predictions begin to deviate from each other after that Reynolds number. They have also found that the upper limit of the laminar flow over the backward facing step is approximately $Re=1000$. The present computations based on the high-order compact implicit

DOI: 10.1002/fld

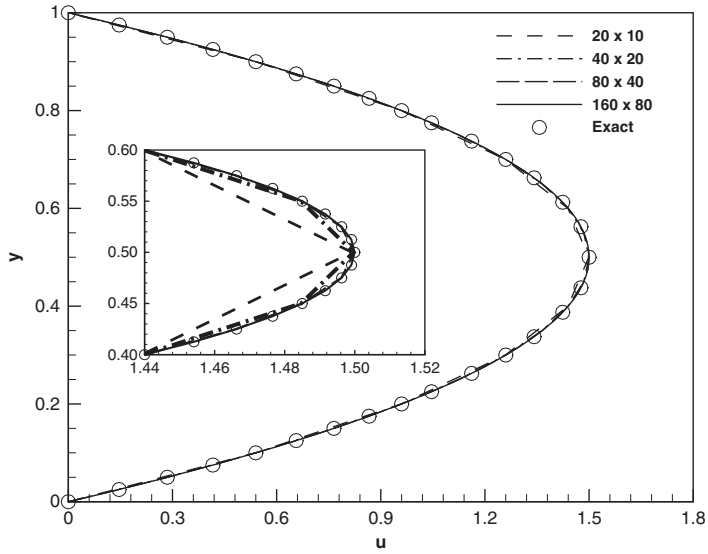

Figure 2. Comparison of the u-velocity profile for the simple channel flow computed by the compact method with the exact solution.

Table III. Order of accuracy of the numerical method implemented based on the L_2 norm of divergence of velocity vector at outlet for simple channel flow.

Grid	Log(Δx)	Log(L_2 norm[Error])
(20×10)	-1.0000000	-6.2814961
(40×20)	-1.3010299	-7.3773581
(80×40)	-1.6020599	-8.5161248
(160×80)	-1.9030899	-9.7438357
Order of accuracy		~3.83

operator scheme are performed for the backward facing step for the Reynolds numbers up to 1200 and the results obtained are compared with the numerical as well as experimental results. A sensitivity study is also performed to examine the effects of the various parameters that may influence the accuracy and convergence rate of the solution. For this test case, the effects of the grid resolution and the pseudocompressibility parameter β on the accuracy and the convergence rate of the solution are studied. In addition, the effects of the filtering parameter a_f and the numerical dissipation coefficient ε_e on the accuracy of the results are discussed. Note that the high-order accurate solutions are computed with the eighth-order filter.

At first, four different computational meshes with uniformly distributed grids are used to examine the sensitivity of the results on the grid resolution and also obtain the order of accuracy of the numerical method implemented. These are the mesh I (150×30), mesh II (300×60), mesh III (600×120) and mesh IV (1200×240). Figure 3 shows a grid refinement study on the wall shear for both the upper and lower walls of the backward facing step flow with $Re=800$. Table IV gives the locations of the separation and reattachment points for the flowfield with $Re=800$ for the different grid sizes. The results demonstrate that the mesh III is suitable for an accurate computation of the flowfield and further grid refinement does not significantly improve the accuracy of the numerical results. Therefore, the mesh III is selected as an appropriate computational grid, regarding the accuracy and the computational effort, for all the present calculations. As shown in Table V, the order of accuracy of the solution for the backward facing step flow is about 3.86, which verifies the fourth-order accuracy of the numerical method implemented. The error is defined as the L_2 norm of the results based on the divergence of the velocity vector for all the grid points for the

DOI: 10.1002/fld

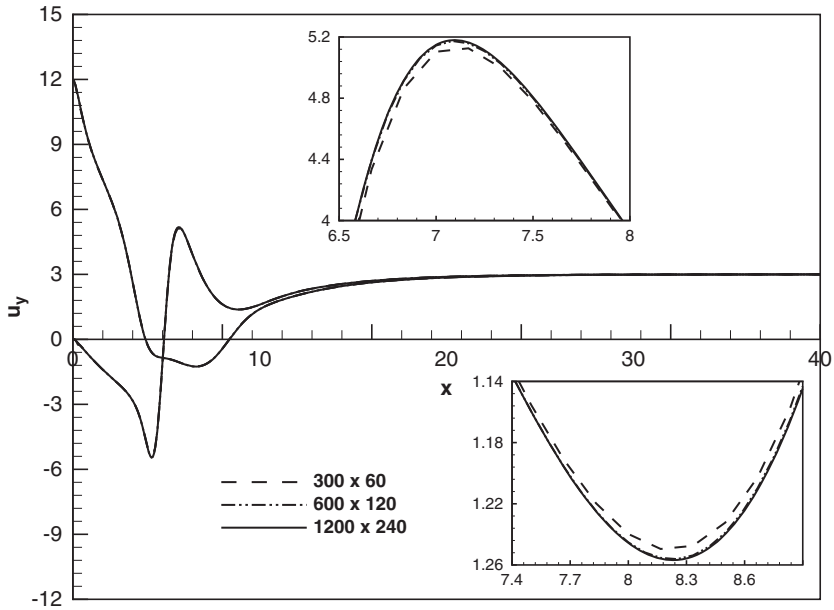

Figure 3. Grid refinement study on the wall shear for both upper and lower walls of backward facing step flow with $Re=800$.

Table IV. Effect of grid refinement on the results of backward facing step flow with $Re=800$, $a_f=0.45$ and $\beta=5$.

Grid	L_1	L_2	L_3
(150×30)	6.1125	4.8745	10.4524
(300×60)	6.1035	4.8632	10.4624
(600×120)	6.0953	4.8530	10.4733
(1200×240)	6.0963	4.8533	10.4772

Table V. Order of accuracy of the numerical method implemented based on L_2 norm of divergence of velocity vector for backward facing step flow with $Re=800$, $a_f=0.45$ and $\beta=5$.

Grid	Δx	$\text{Log}(\Delta x)$	$\text{Log}(L_2\,\text{norm[Error]})$
(150×30)	50/150	−0.47712	−6.2578
(300×60)	50/300	−0.7781	−7.4306
(600×120)	50/600	−1.0791	−8.5834
Order of accuracy			∼3.86

meshes (150×30), (300×60) and (600×120), compared with the results of the most refined one, i.e. the mesh (1200×240). The above results are obtained using the filtering parameter $a_f=0.45$ and the pseudocompressibility parameter $\beta=5$.

The effects of the numerical dissipation value ε_e and the filtering coefficient α_f on the flowfield characteristics are studied herein, as shown in Figures 4 and 5. The results are presented for the two computational meshes (the meshes II and III). It is found that the accuracy of the solution computed based on the high-order compact method employed is sensitive to the grid size and the numerical dissipation value. The study shows that a larger value of ε_e especially for coarse grid affects the solution. The results indicate that with increasing the number of grid points, the value of numerical dissipation does not have a significant influence on the solution. It is found that the

DOI: 10.1002/fld

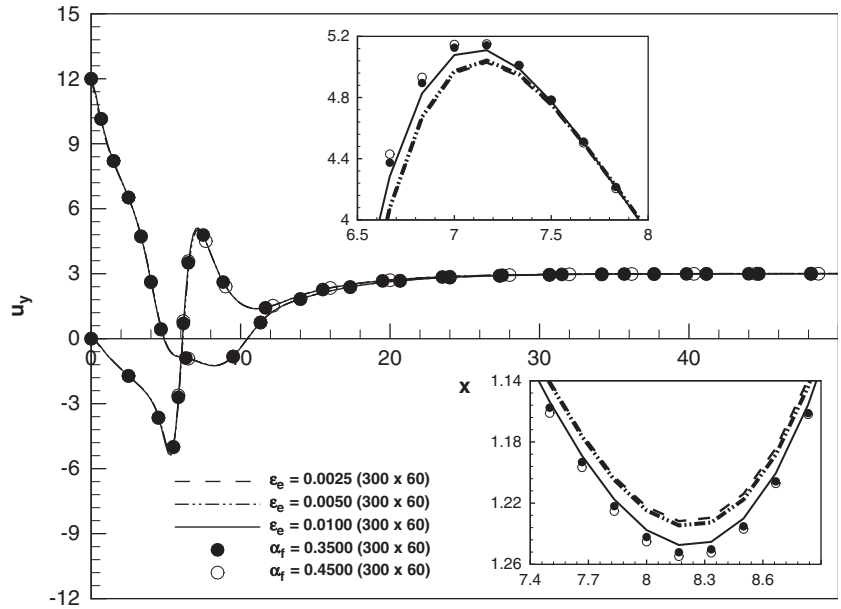

Figure 4. Effect of dissipation value ε_e and filter coefficient a_f on the wall shear for both upper and lower walls of backward facing step flow with $Re=800$ for grid (300×60) and $\beta=5$.

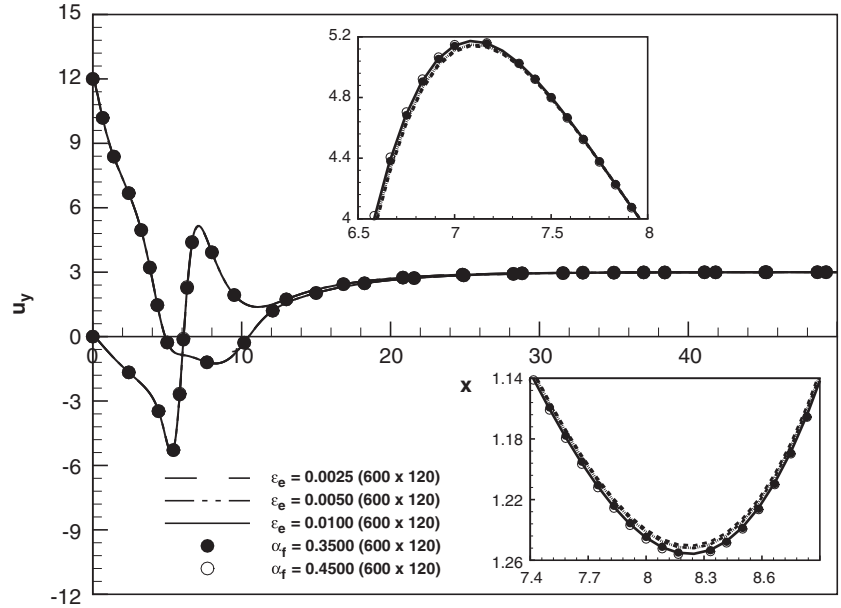

Figure 5. Effect of dissipation value ε_e and filter coefficient a_f on the wall shear for both upper and lower walls of backward facing step flow with $Re=800$ for grid (600×120) and $\beta=5$.

results of wall shear obtained from the filtering procedure are less sensitive to grid size. It has been shown that the calculated results for the locations of the separation and reattachment points (L_1, L_2, L_3 see Figure 1) are not very sensitive to the filtering coefficient. The study has indicated that the filtering coefficient in the range $\alpha_f \geqslant 0.45$ gives the reasonable results. It is demonstrated that the performance of the filtering procedure is better than the sixth-order numerical dissipation terms implemented in the solution algorithm for the backward facing step test case. The results have also revealed that the convergence rate of the solution is unaffected by the values of the

DOI: 10.1002/fld

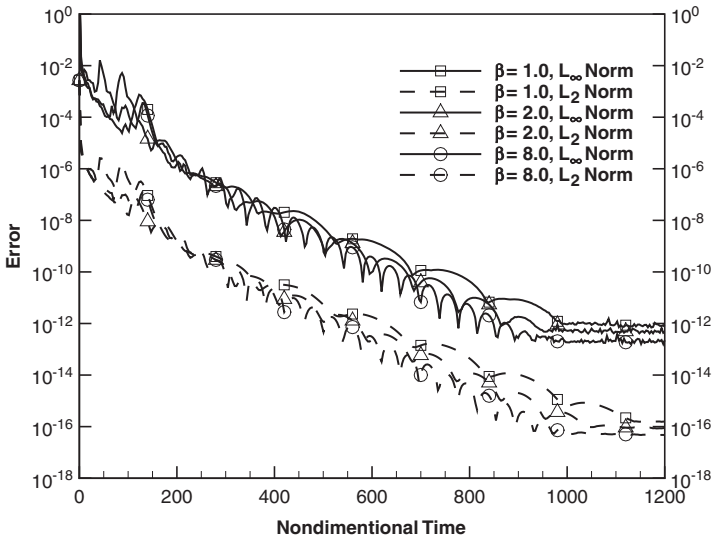

Figure 6. Convergence history of the solution based on the divergence of the velocity vector for backward facing step flow for different values of pseudocompressibility parameter β with $Re=800$.

filtering parameter a_f. A comparison between the results obtained by the sixth- and eight-order filters also indicated that the order of filter does not affect the accuracy of the solution.

The effects of the pseudocompressibility parameter β on the accuracy and the convergence rate of the solution are studied herein for the mesh III and $Re=800$. It is found that the results are not very sensitive to the value of the pseudocompressibility parameter β. The study has shown that very small or large values of β slow down the solution convergence considerably. Figure 6 shows that the values of the pseudocompressibility parameter β in the range of $2-10$ give a faster convergence for the backward facing step flow. In this figure, the error is calculated based on the divergence of the velocity vector that indicates the direct evidence of divergence-free solution for the backward facing step flow case. Note that the best value of the artificial compressibility parameter β depends on the characteristic velocity in the flowfield, and therefore, the value of the optimum β changes when the characteristic velocity varies. Figure 7 indicates that with increasing *Re*, the convergence rate of the solution decreases and more iterations are needed for the solution to be converged. The same trend has been seen in the cavity problem. This may be due to the central differencing of the convective terms of the governing equations and also dropping the viscous terms in the left-hand side of the compact formulation, results in low dissipation of the compact method used. For high Reynolds number flows, one can use an upwind-biased algorithm for differencing of the convective terms instead of the central scheme. It may alleviate the problem, because upwind compact methods have higher dissipation amounts compared to central compact ones.

The flow for the backward facing step for different Reynolds numbers is studied in more detail. Table VI gives the computed results for the locations of the separation and reattachment points for $200\leqslant Re\leqslant 1200$. These flowfield parameters can be obtained from the computed wall shear $\partial u/\partial y$ for the upper and lower walls where $\partial u/\partial y=0$ (see Figure 8). Figure 9 illustrates the computed flowfield for the backward facing step shown by the velocity profiles and streamlines for $200\leqslant Re\leqslant 1200$ while Figure 10 gives the pressure contours. It can be seen, as the Reynolds number increases, the flowfield for the backward facing step becomes more complex. The present results show the appearance of the second recirculating zone (the secondary vortex) at Reynolds number about 400, which agrees with the measurements by Armaly *et al.* [28] and computation by Rogers and Kwak [29], Mawlood *et al.* [30] and Marinova *et al.* [31]. But Kim and Moin [32] have reported the appearance of the secondary bubble at Reynolds number 600. Note that the secondary vortex is a consequence of the adverse pressure gradient appears for Reynolds number larger than 400, as shown in Figure 10. It can be seen for the range $Re\leqslant 400$ in which the two-dimensionality of the flow retains, the fourth-order compact method implemented indicates

DOI: 10.1002/fld

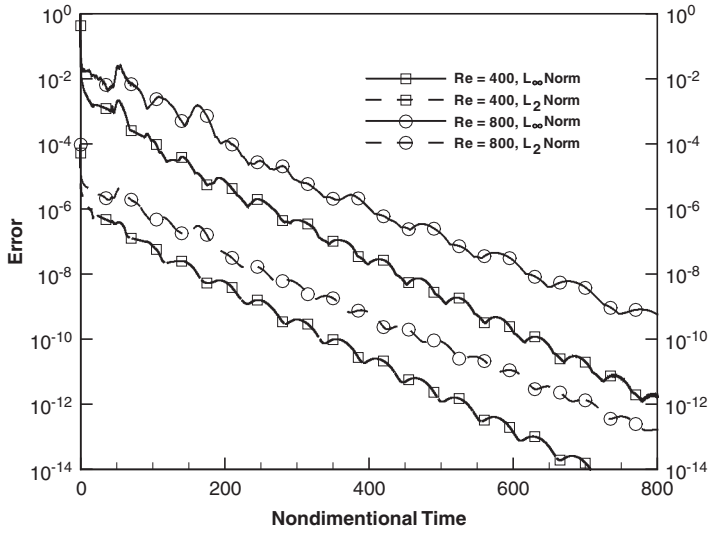

Figure 7. Convergence history of the solution for backward facing step flow with $Re=400$ and 800.

Table VI. Effect of Reynolds number on the results of backward facing step flow for grid (600×120), $\beta=5$ and $a_f=0.45$.

Re	L_1	L_2	L_3
200	2.6660	—	—
300	3.5683	—	—
400	4.3221	4.0084	5.1865
500	4.9148	4.1459	6.7664
600	5.3725	4.3748	8.1070
700	5.7515	4.6109	9.3267
800	6.0953	4.8530	10.4733
900	6.4146	5.0931	11.5716
1000	6.7231	5.3364	12.6353
1100	7.0167	5.5754	13.6640
1200	7.2994	5.8108	14.6565

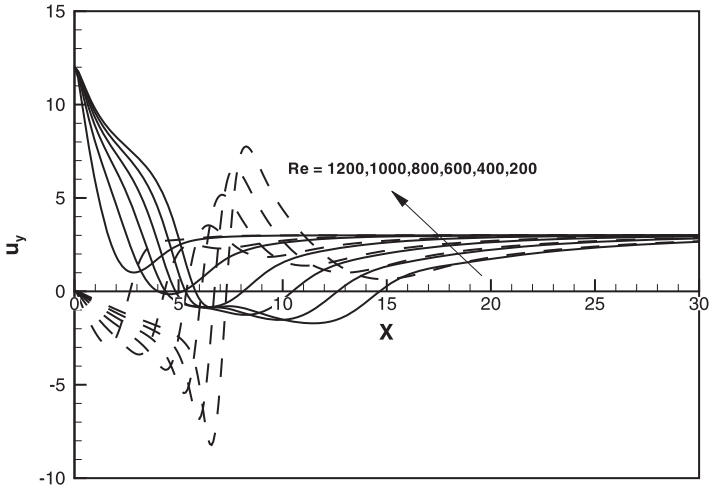

Figure 8. Comparison of wall shear for both upper and lower walls of backward facing step flow with $Re=200$, 400, 600, 800, 1000 and 1200.

DOI: 10.1002/fld

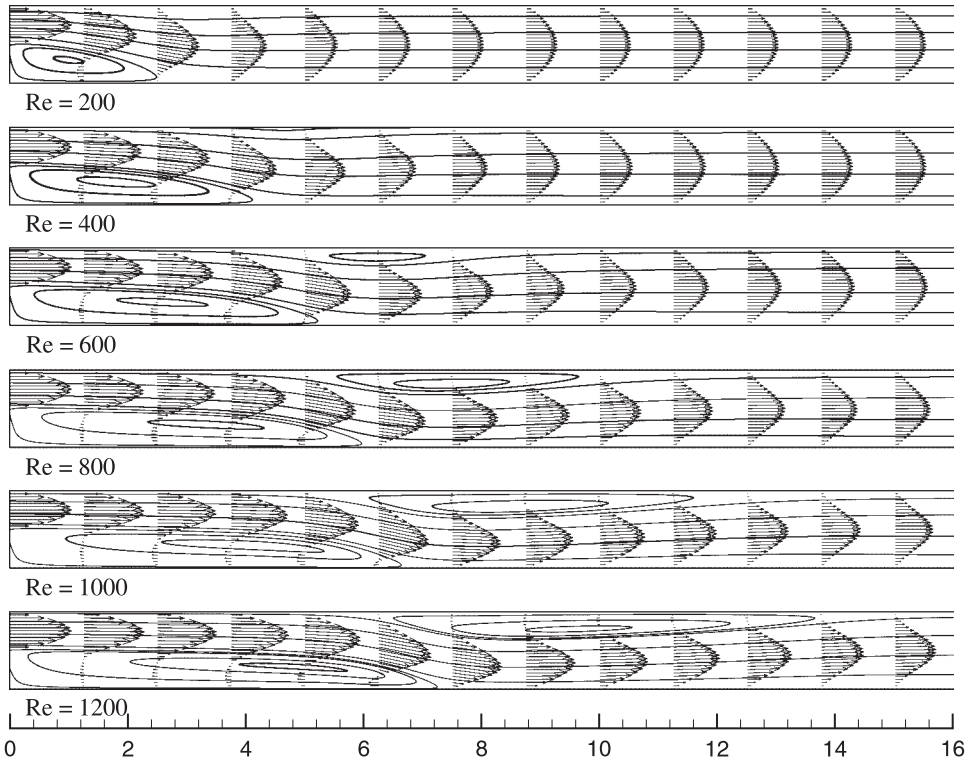

Figure 9. Computed flowfield for backward facing step shown by velocity profiles and streamlines with $Re = 200$, 400, 600, 800, 1000 and 1200.

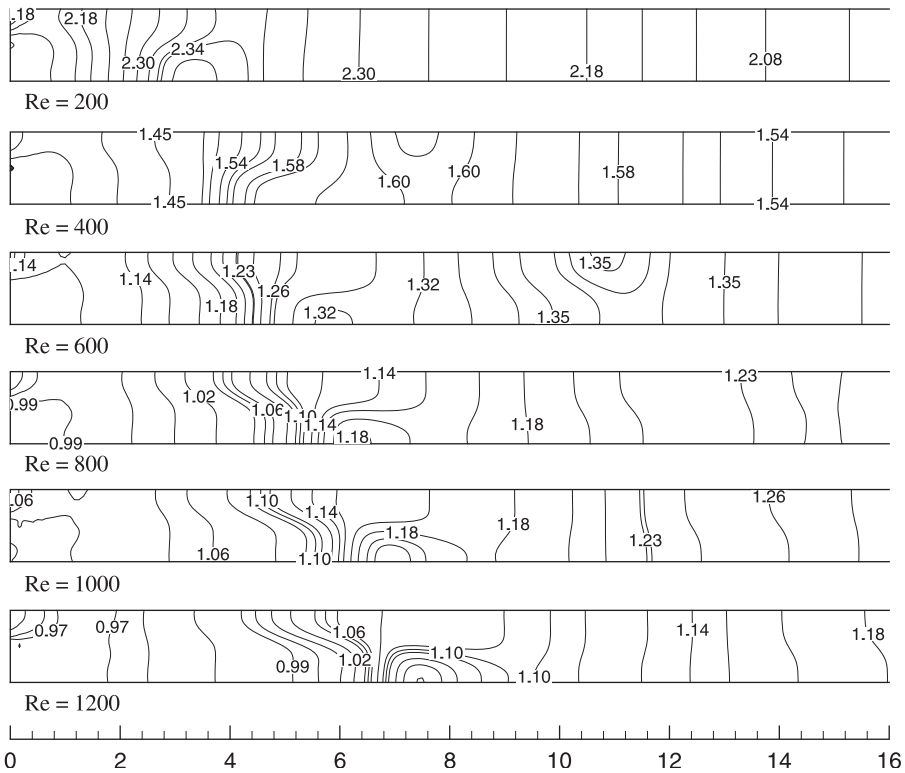

Figure 10. Computed flowfield for backward facing step shown by pressure contours with $Re = 200$, 400, 600, 800, 1000 and 1200.

DOI: 10.1002/fld

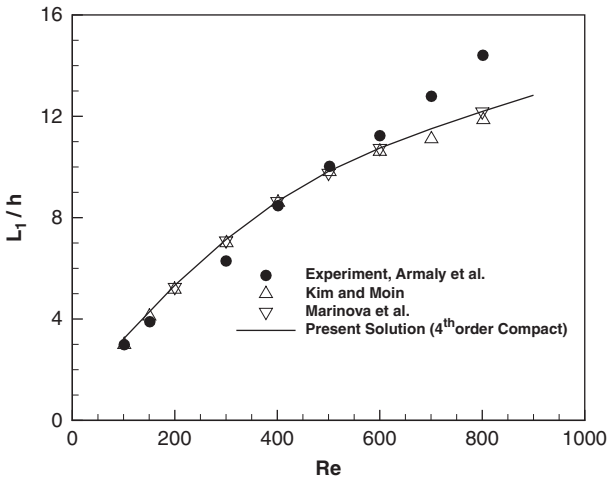

Figure 11. Comparison of reattachment location for backward facing step flow with different *Re*.

Table VII. Comparison of the present solution with the available results for backward facing step flow for $Re = 800$.

Work	L_1	L_2	L_3	Node
Barton	6.015	4.82	10.48	—
Gartling	6.10	4.85	10.48	129 681
Gresho *et al.* (FD)	6.082	4.8388	10.4648	245 760
Gresho *et al.* (SE)	6.10	4.86	10.49	$\geqslant$8000
Marinova *et al.*	6.0909	4.8214	10.4719	65 536
Keskar and Lyn	6.0964	4.8534	10.4785	3737
Present solution	6.0953	4.8530	10.4733	72 000

good agreement with the experiment. With the formation of the second recirculating flow region for $Re \geqslant 400$, the flowfield becomes three-dimensional and the numerical results deviate from those of the experiment; however, the results obtained by the compact method show better agreement with the results of other two-dimensional numerical methods for $Re \geqslant 400$ (see Figure 11).

For examining the accuracy of the solution for this problem, a comparison is made between the present results and others for $Re = 800$ on the mesh III, as shown in Table VII. This table gives the present computations for the locations of the separation and reattachment points, which show good agreement compared with the spectral solution by Keskar and Lyn [33] and also other numerical results based on the different numerical methods [37–39]. The present numerical procedure based on the fourth-order compact implicit operator method exhibits a good robustness for solving steady incompressible viscous flows for different Reynolds numbers and obtains accurate and efficient solutions in comparison with the experimental and numerical results.

7.2. Flow in a two-dimensional cavity

A classical steady-state flow problem with well-defined boundary conditions is the square lid-driven cavity flow. This problem is served as a benchmark case for examining accuracy and efficiency of numerical methods implemented to solve incompressible flows. The boundary conditions used for this case consist of a zero normal pressure gradient for all walls and noslip conditions for the velocity components ($u = v = 0$) for all boundaries except for the upper wall where $u = 1$ and $v = 0$. The computations are carried out for the flow conditions $Re = 100$,1000, 3200 and 5000 on different computational meshes to examine the sensitivity of the results on the grid size. The computational grids used herein for the calculations are $(I\max, J\max) = (61, 61)$, $(101, 101)$, $(161, 161)$, $(201, 201)$. All computations based on the high-order compact

DOI: 10.1002/fld

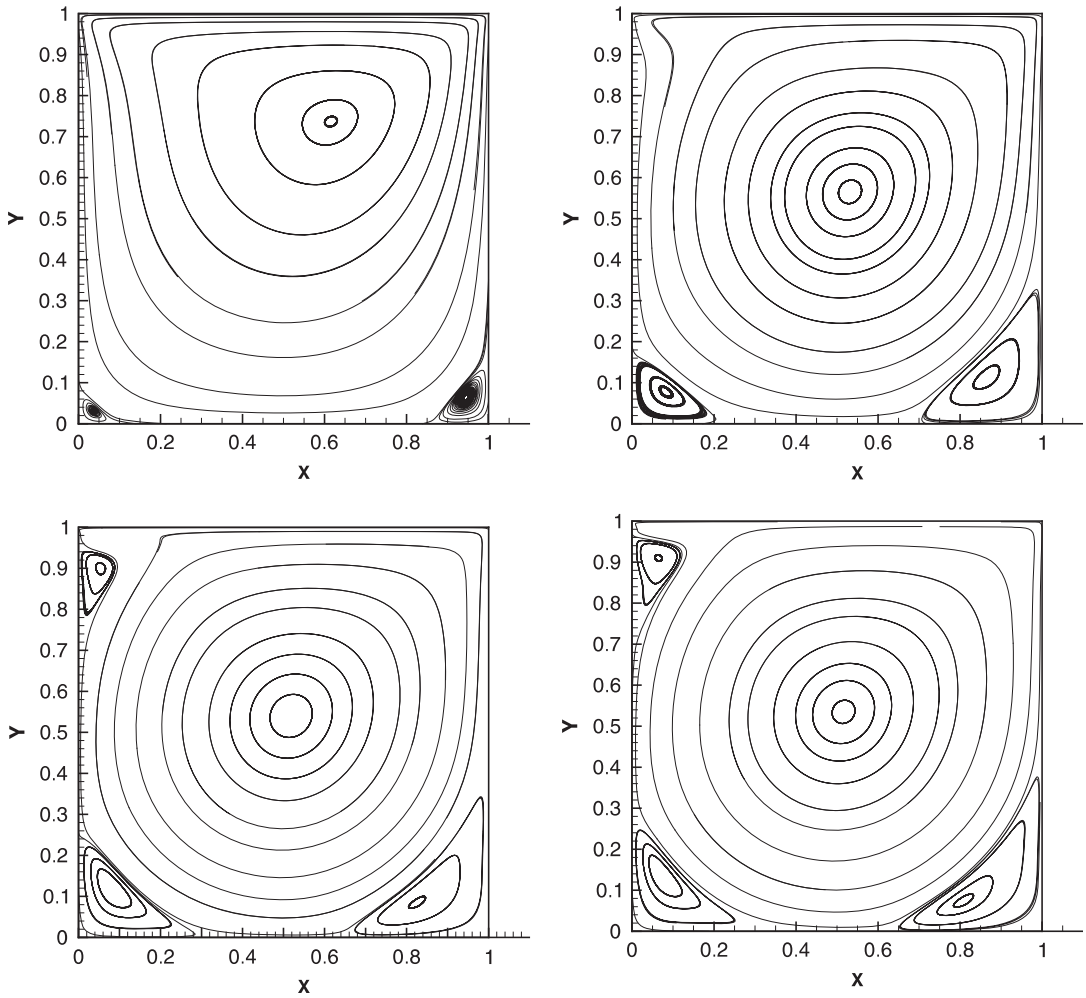

Figure 12. Computed flowfield for 2-D cavity shown by streamlines with $Re=100$ (first row, left), 1000 (first row, right), 3200 (second row, left) and 5000 (second row, right).

scheme used are performed with the eighth-order filter and the filtering parameter is set to be $a_f=0.45$.

Figure 12 gives the computed flowfield shown by the streamlines using the high-order compact method for the cavity for $Re=100$, 1000, 3200 and 5000. Both the u-velocity profile along the vertical line and the v-velocity profile along the horizontal line passing through the center of the cavity for each case are shown in Figure 13. The study shows that the results of the compact method implemented are not very sensitive to the grid size for moderate Re. For $Re=100$ and 1000, the grid (101×101) is the appropriate one for an accurate calculation of the flowfield. The accurate computation of the flow filed for a higher Reynolds number, $Re=3200$ or 5000, needs a higher number of grid points, i.e. (161×161) or (201×201). The present results using the high-order compact method are compared with the second-order accurate solution by Ghia *et al.* [40] and the fourth-order accurate solutions by Ekaterinaris [9] and Ertirk *et al.* [41], which exhibit good agreement. Figure 14 illustrates the convergence history of the solution for both the L_2 norm and L_∞ norm (maximum norm) based on the velocity variable in the flowfield for $Re=100$. The effect of the pseudocompressibility parameter β, which can control the solution convergence, is also investigated in this figure. The study has indicated that the values of the artificial compressibility parameter β in the range of $2-10$ give a faster convergence to the steady-state solution for moderate Re and very small or large values of β slow down the solution convergence. It was also found that the results are not very sensitive to the value of the pseudocompressibility parameter

DOI: 10.1002/fld

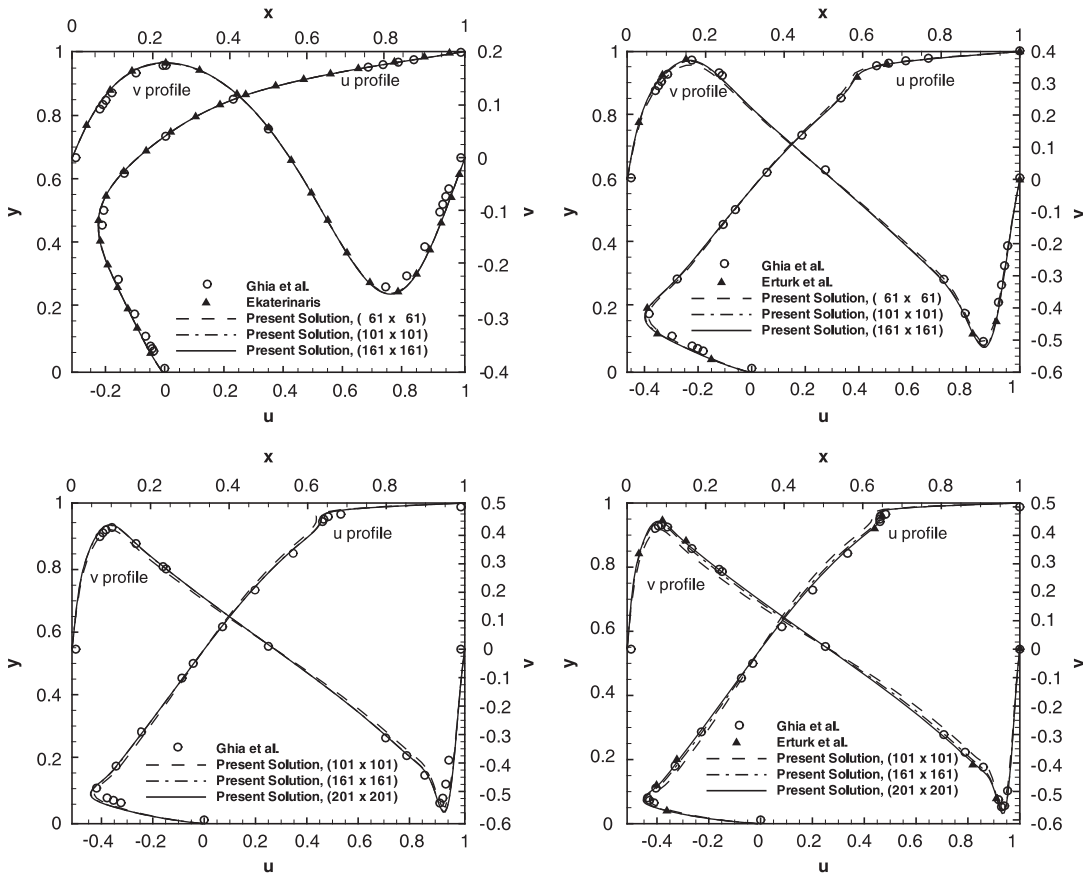

Figure 13. Comparison of velocity profiles at the mid-planes for 2-D cavity flow with $Re = 100$ (first row, left), 1000 (first row, right), 3200 (second row, left) and 5000 (second row, right).

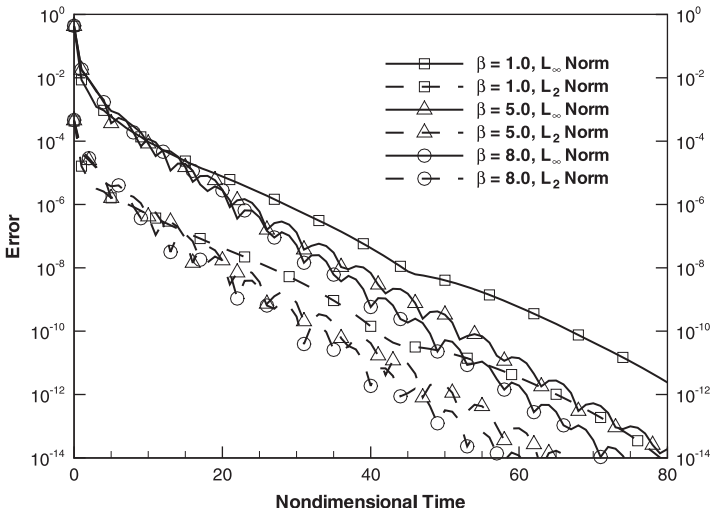

Figure 14. Convergence history of the solution for 2-D cavity flow for different values of pseudocompressibility parameter β with $Re = 100$.

β for moderate Re. For high Re, the accuracy of the results slightly depends on the artificial compressibility parameter β, and a larger value of β than the mentioned range provides a more accurate solution.

DOI: 10.1002/fld

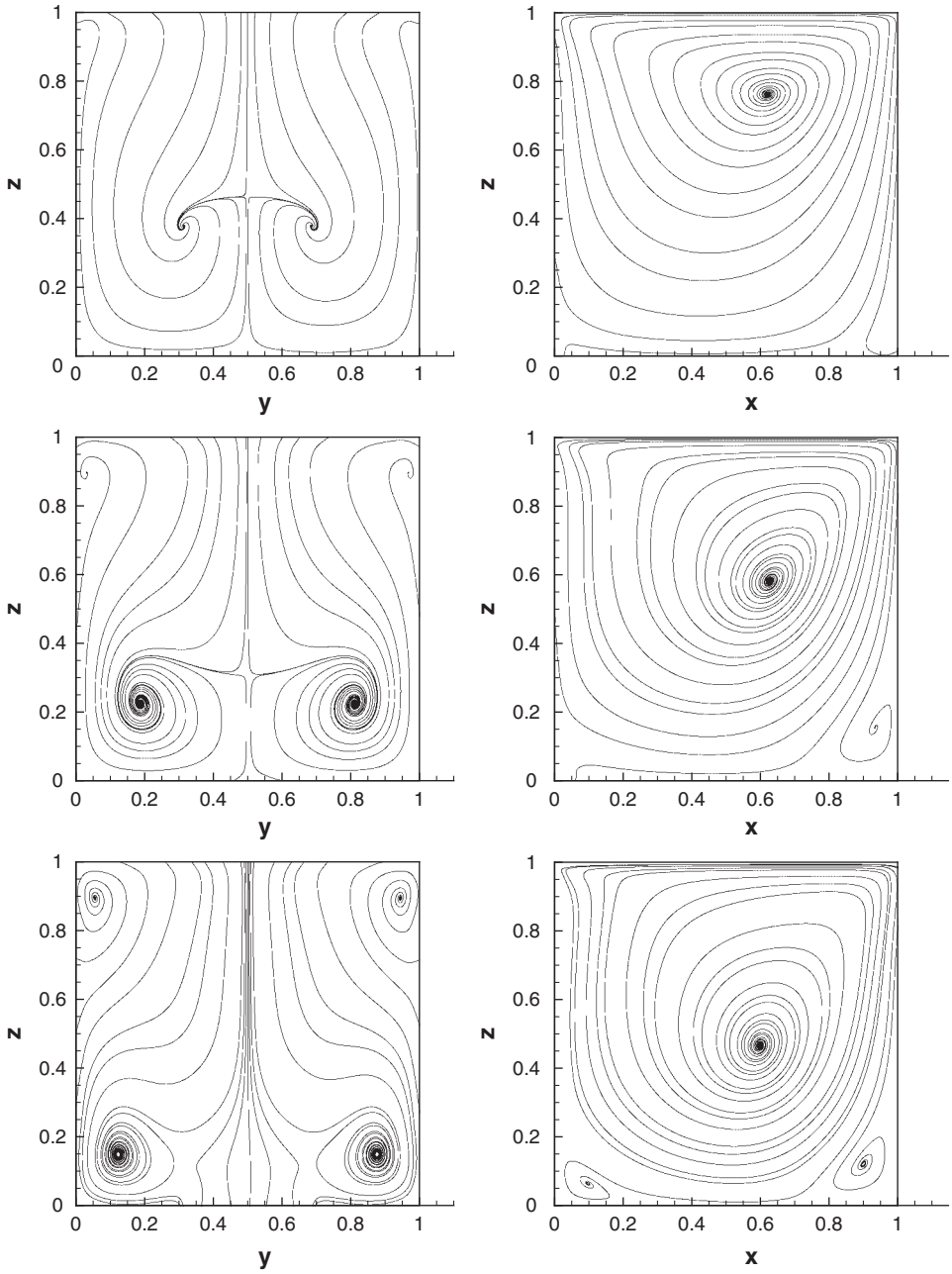

Figure 15. Computed flowfield for 3-D cavity shown by streamlines at the planes $x=0.5$ and $y=0.5$ for $Re=100$ (top), 400 (middle) and 1000 (bottom).

7.3. Flow in a three-dimensional cavity

Herein, the 3-D high-order accurate developed code is used to compute the flow in a cubic cavity. The noslip boundary conditions ($u=v=w=0$) are used for all velocity components on all walls except for the upper wall ($u=1, v=w=0$). The calculations are performed for the different flow conditions ($Re=100, 400, 1000$) and for the two computational grids, namely ($30\times30\times30$) and ($40\times40\times40$). The pseudocompressibility parameter is chosen to be $\beta=5$ and the filter coefficient is set to be $\alpha_f=0.45$ for all cases considered.

Figure 15 shows the computed flowfield shown by the streamlines in the $y-z$ ($x=0.5$) and $x-z$ ($y=0.5$) planes for the cases considered, $Re=100, 400, 1000$. As shown in this figure, due

DOI: 10.1002/fld

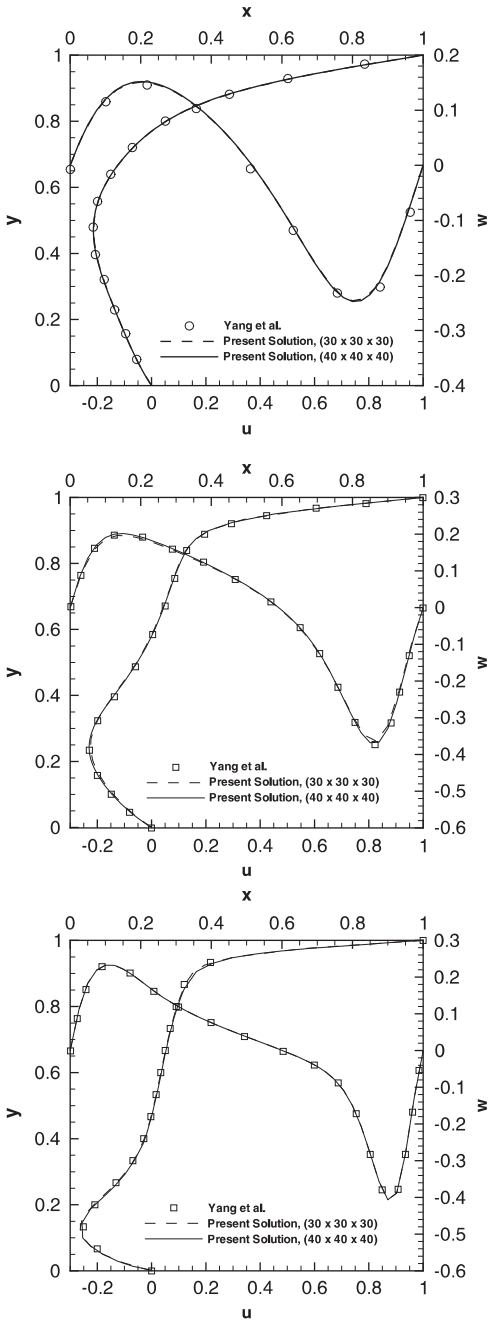

Figure 16. Comparison of velocity profiles at the mid-planes $x=y=0.5$ and $y=z=0.5$ for 3-D cavity flow for $Re=100$ (top), 400 (middle) and 1000 (bottom).

to the effect of the side walls, the flow patterns in the $y-z$ plane show a pair of counterrotating vortices. In addition, a pair of small counterrotating vortices can be seen near the upper corners. The results indicate that with increasing *Re*, the centers of the centered vortices are considerably moved toward the lower wall and the vortices near the corners grow. The primary recirculating region and also secondary vortices near the corners in the $x-z$ plane can also be seen for each case. It can be seen that with increasing *Re*, the center of the primary vortex is moved toward the center of the cavity, as seen in the 2-D cavity flow. The present computations using the high-order compact method for the velocity components (u, w) at the mid-planes $x=y=0.5$ and $y=z=0.5$, respectively, are compared with the results by Yang *et al.* [42], as shown in Figure 16. The results

DOI: 10.1002/fld

based on the high-order compact method for the three cases $Re=100, 400, 1000$ are in good agreement with those of Yang *et al.*. It is obvious that the results obtained by the compact method for the two computational grids, $(30\times30\times30)$ and $(40\times40\times40)$, are nearly the same, which show the accuracy of the numerical method implemented.

8. CONCLUSION

A fourth-order compact finite-difference scheme is used for solving steady incompressible flows. The high-order compact method applied is an alternating direction implicit operator scheme which is efficiently implemented to compute the incompressible Navier–Stokes equations in the primitive variables formulation using the artificial compressibility method. For space discretizing the convective fluxes, fourth-order centered spatial accuracy of the implicit operators is efficiently obtained by performing compact space differentiation in which the method takes advantage of block-tridiagonal matrix inversions. High-order spectral-type low-pass compact filters and/or numerical dissipation terms are utilized to stabilize the instability of the numerical method implemented. The study indicates that the results are sensitive to the numerical dissipation value and are not very sensitive to the filtering coefficient. It is found that by increasing the number of grid points, the effect of numerical dissipation becomes very less important. It is demonstrated that the performance of the filtering procedure is better than the numerical dissipation terms implemented in the solution algorithm. In the present study, the high-order compact implicit operator scheme is also extended for computing three-dimensional incompressible flows. The calculations are performed for different incompressible flow problems to demonstrate the accuracy and efficiency of the high-order compact implicit operator scheme used. The computed results agree very well with the available numerical and experimental results. The present computations indicate that the high-order compact implicit operator scheme used is robust, efficient and accurate for solving 2-D and 3-D incompressible flow problems.

APPENDIX A

Here, the stability analysis of the fourth-order compact scheme for the two- and three-dimensional linear advection equations is performed with the sixth-order numerical dissipation term added to the differenced equation. In [43], a stability analysis for the one-dimensional advection–diffusion equation is performed with the sixth-order numerical dissipation added to the differenced equation and the stability band was obtained ($0\leqslant\varepsilon_e\leqslant1/32$). In the following, we use the Von-Neumann stability analysis for the three-dimensional advection equation, $u_t+a(u_x+u_y+u_z)=0$. Consider the three-dimensional linear advection equation with the sixth-order dissipation term added to the right-hand side of the equation

$$u_t+a(u_x+u_y+u_z)=\varepsilon_e\left(\frac{(\Delta x)^6}{(\Delta t)}u_{xxxxxx}+\frac{(\Delta y)^6}{(\Delta t)}u_{yyyyyy}+\frac{(\Delta z)^6}{(\Delta t)}u_{zzzzzz}\right) \tag{A1}$$

Using the compact differencing (Equation (16)) for the space discretization in the x-, y- and z- directions, and the Euler implicit method for the time-marching scheme and also using the operator notation, we have

$$u^{n+1}-u^n+r_xQ_x^{-1}D_xu^{n+1}+r_yQ_y^{-1}D_yu^{n+1}+r_zQ_z^{-1}D_zu^{n+1}=\varepsilon_e[(\Delta\nabla)_x^3+(\Delta\nabla)_y^3+(\Delta\nabla)_z^3]u^n,$$

$$r_x=\frac{a\Delta t}{\Delta x},\quad r_y=\frac{a\Delta t}{\Delta y},\quad r_z=\frac{a\Delta t}{\Delta z}$$

$$Q_xu_i=\frac{u_{i+1,j,k}+4u_{i,j,k}+u_{i-1,j,k}}{6},\quad D_xu_i=\frac{u_{i+1,j,k}-u_{i-1,j,k}}{2},$$

DOI: 10.1002/fld

$$
\begin{aligned}
(\Delta\nabla)_x &= u_{i+1,j,k}-2u_{i,j,k}+u_{i-1,j,k}\\
Q_y u_j &= \frac{u_{i,j+1,k}+4u_{i,j,k}+u_{i,j-1,k}}{6}, \quad D_y u_j = \frac{u_{i,j+1,k}-u_{i,j-1,k}}{2},\\
(\Delta\nabla)_y &= u_{i,j+1,k}-2u_{i,j,k}+u_{i,j-1,k}\\
Q_z u_k &= \frac{u_{i,j,k+1}+4u_{i,j,k}+u_{i,j,k-1}}{6}, \quad D_z u_k = \frac{u_{i,j,k+1}-u_{i,j,k-1}}{2},\\
(\Delta\nabla)_z &= u_{i,j,k+1}-2u_{i,j,k}+u_{i,j,k-1}
\end{aligned}
\tag{A2}
$$

By applying the Von-Neumann stability analysis, the amplification factor can be obtained

$$
\begin{aligned}
u^n_{i,j,k} &= \sum \widehat{u}^n_{i,j,k} \mathrm{e}^{Jik_m x} \mathrm{e}^{Jjk_l y} \mathrm{e}^{Jkk_n z}, \quad J=\sqrt{-1}\\
G &= \left|\frac{\widehat{u}^{n+1}_{i,j,k}}{\widehat{u}^n_{i,j,k}}\right| = \frac{\left(\varepsilon_e[(\Delta\nabla)^3_x+(\Delta\nabla)^3_y+(\Delta\nabla)^3_z]+1\right)\mathrm{e}^{Jik_m x}\mathrm{e}^{Jjk_l y}\mathrm{e}^{Jkk_n z}}{(1+r_x Q_x^{-1} D_x + r_y Q_y^{-2} D_y + r_z Q_z^{-2} D_z)\mathrm{e}^{Jik_m x}\mathrm{e}^{Jjk_l y}\mathrm{e}^{Jkk_n z}}\\
&= \frac{Q_x Q_y Q_z(\varepsilon_e[(\Delta\nabla)^3_x+(\Delta\nabla)^3_y+(\Delta\nabla)^3_z]+1)}{(Q_x Q_y Q_z + r_x Q_y Q_z D_x + r_y Q_x Q_z D_y + r_z Q_x Q_y D_z)}\\
&= \frac{(\varepsilon_e[(2\cos\alpha-2)^3+(2\cos\beta-2)^3+(2\cos\gamma-2)^3]+1)}{1+J(C_x r_x + C_y r_y + C_z r_z)}\\
C_x &= \left(\frac{\cos\beta+2}{3}\right)^{-1}\left(\frac{\cos\gamma+2}{3}\right)^{-1}\sin\beta\sin\gamma\\
C_y &= \left(\frac{\cos\alpha+2}{3}\right)^{-1}\left(\frac{\cos\gamma+2}{3}\right)^{-1}\sin\alpha\sin\gamma\\
C_z &= \left(\frac{\cos\alpha+2}{3}\right)^{-1}\left(\frac{\cos\beta+2}{3}\right)^{-1}\sin\alpha\sin\beta\\
0<\alpha &= k_m\Delta x<\pi, \quad 0<\beta=k_l\Delta y<\pi, \quad 0<\gamma=k_n\Delta z<\pi
\end{aligned}
\tag{A3}
$$

For stability we need $|G|\leqslant 1$. Since r_x, r_y and r_z appeared in the imaginary part of the denominator, increasing r_x, r_y and r_z decreases $|G|$. As a result, if $|G|\leqslant 1$ for $r_x=r_y=r_z=0$, then $|G|\leqslant 1$ for all r_x, r_y and $r_z\in\mathbb{R}$. In the other words, stability for $r_x=r_y=r_z=0$ is sufficient for stability of all r_x, r_y and $r_z\in\mathbb{R}$. Considering this statement, we study the stability condition for $r_x=r_y=r_z=0$. Therefore, we have

$$
|G| = |(\varepsilon_e[(2\cos\alpha-2)^3+(2\cos\beta-2)^3+(2\cos\gamma-2)^3]+1)|\leqslant 1 \tag{A4}
$$

The maximum of the above function occurs at $\alpha=\beta=\gamma=\pi$, and therefore, the stability band for the sixth-order numerical dissipation term added to the differenced equation is found as follows

$$
0\leqslant\varepsilon_e\leqslant\frac{1}{96} \tag{A5}
$$

The same procedure can be used for the two-dimensional linear advection equation and the stability band for the sixth-order numerical dissipation coefficient is obtained as follows

$$
0\leqslant\varepsilon_e\leqslant\frac{1}{64} \tag{A6}
$$

ACKNOWLEDGEMENTS

The authors thank Sharif University of Technology for financial support of this research.

DOI: 10.1002/fld

REFERENCES

1. Gupta MM. High accuracy solutions of incompressible Navier–Stokes equations. *Journal of Computational Physics* 1991; **93**:343–359.
2. Weaseling P. Multigrid solution of the Navier–Stokes equations in the vorticity-streamfunction formulation. In *Efficient Solutions of Elliptic Systems*, Hackbusch W (ed.). Notes on Numerical Fluid Mechanics, vol. 10. Vieweg: Braunschweig, 1984; 145–154.
3. Chorin AJ. A numerical method for solving incompressible viscous flow problems. *Journal of Computational Physics* 1967; **2**:12–26.
4. Morinishi Y, Lund TS, Vasilyev OV, Moin P. Fully conservative higher order finite difference schemes for incompressible flow. *Journal of Computational Physics* 1998; **143**:90–124.
5. Mahesh K, Constantinescu G, Moin P. A numerical method for large-eddy simulation in complex geometries. *Journal of Computational Physics* 2004; **197**:215–240.
6. Chen GQ, Gao Z, Yang ZF. A perturbational h^4 exponential finite difference scheme for the convective diffusion equation. *Journal of Computational Physics* 1993; **104**:129–139.
7. Dennis SCR, Hudson JD. Compact h^4 finite-difference approximations to operators of Navier–Stokes type. *Journal of Computational Physics* 1989; **85**:390–416.
8. Li M, Tang T, Fornberg B. A compact fourth-order finite difference scheme for the steady incompressible Navier–Stokes equations. *International Journal for Numerical Methods in Fluids* 1995; **20**:1137–1151.
9. Ekaterinaris JA. High-order accurate numerical solutions of incompressible flows with the artificial compressibility method. *International Journal for Numerical Methods in Fluids* 2004; **45**:1187–1207.
10. E W, Liu J-G. Essentially compact schemes for unsteady viscous incompressible flows. *Journal of Computational Physics* 1996; **126**:122–138.
11. Karniadakis GE, Sherwin SJ. *Spectral/hp Element Method for CFD*. Oxford University Press: Oxford, 1999.
12. Ekaterinaris JA. Implicit high-order accurate in space algorithms for the Navier–Stokes equations. *AIAA Journal* 2000; **38**(6):1594–1602.
13. Ekaterinaris JA. Implicit, high-resolution, compact schemes for gas dynamics and aeroacoustics. *Journal of Computational Physics* 1991; **156**:272–299.
14. Khajeh-Saeed A. Numerical simulation of incompressible Newtonian/non-Newtonian fluid flows using a high-order compact implicit operator scheme with artificial compressibility method. *MSc Thesis*, Sharif University of Technology, January 2007.
15. Hejranfar K, Khajeh-Saeed A. A high-order accurate implicit operator scheme for solving incompressible viscous flows using artificial compressibility method. *The Fifth International Conference on Computational Fluid Dynamics* (*ICCFD5*), Seoul, Korea, July 2008.
16. Merkle CL, Athavale M. Time-accurate unsteady incompressible flow algorithm based on artificial compressibility. *AIAA Paper* 1987; 87–1137.
17. Malan AG, Lewis RW, Nithiarasu P. An improved unsteady, unstructured, artificial compressibility, finite volume scheme for viscous incompressible flows: part I. Theory and implementation. *International Journal for Numerical Methods and Engineering* 2002; **54**:695–714.
18. Rizzi A, Eriksson LE. Computation of inviscid incompressible flow with rotation. *Journal of Fluid Mechanics* 1985; **153**:275–312.
19. Beam RM, Warming RF. An implicit factored scheme for the compressible Navier–Stokes equation. *AIAA Journal* 1978; **16**(4):393–402.
20. Hirsch SR. Higher order accurate difference solutions of fluid mechanics problems by a compact differencing technique. *Journal of Computational Physics* 1975; **19**:90–109.
21. Lele SK, Tatineni M. Compact finite different schemes with spectral-like resolution. *Journal of Computational Physics* 1992; **103**:16–42.
22. Visbal MR, Gaitonde DV. On the use of higher-order finite-difference schemes on curvilinear and deforming meshes. *Journal of Computational Physics* 2002; **181**:155–185.
23. Visbal MR, Gaitonde DV. High-order accurate methods for complex unsteady subsonic flows. *AIAA Journal* 1999; **37**(10):1231–1239.
24. Gaitonde DV, Shang JS, Young JL. Practical aspects of higher-order numerical schemes for wave propagation phenomena. *International Journal for Numerical Methods and Engineering* 1999; **45**:1849–1869.
25. Gaitonde DV, Visbal MR. Further development of a Navier–Stokes solution procedure based on higher-order formulas. *Technical Paper 99-0557*. AIAA Press: Washington, DC, 1999.
26. Carpenter MH, Gottlieb D, Abarbanel S. The stability of numerical boundary treatments of compact high-order finite-difference schemes. *Journal of Computational Physics* 1993; **108**:272–295.
27. Vichenevetsky R, Bowles JB. *Fourier Analysis of Numerical Approximations of Hyperbolic Equations*. SIAM Studies in Applied Mathematics. SIAM: Philadelphia, 1982.
28. Armaly BF, Durst F, Pereira JCF, Schonung B. Experimental and theoretical investigation of backward-facing step flow. *Journal of Fluid Mechanics* 1983; **127**:473–496.
29. Rogers SE, Kwak D. An upwind differencing scheme for the incompressible Navier–Stokes equations. *Applied Numerical Mathematics* 1991; **8**:43–64.
30. Mawlood Mahmood K, Asrar W, Omar AA, Basri SN. Flow past a backward facing step: fourth-order compact finite difference results. *32nd AIAA Fluid Dynamics Conference and Exhibit*, St. Louis, Missouri, 24–26 June 2002.

DOI: 10.1002/fld

31. Marinova RS, Christov CI, Marinova TT. A fully coupled solver for incompressible Navier–Stokes equations using operator splitting. *International Journal of Computational Fluid Dynamics* 2003; **17**:371–385.
32. Kim J, Moin P. Application of fractional-step method to incompressible Navier–Stokes equations. *Journal of Computational Physics* 1985; **59**:308–323.
33. Keskar J, Lyn DA. Computations of a laminar backward-facing step flow at Re = 800 with a spectral domain decomposition method. *International Journal for Numerical Methods in Fluids* 1999; **29**:411–427.
34. Thangam S, Knight DD. Effect of stepheight on the separated flow past a backward facing step. *Physics of Fluids* 1989; **A1**(3):604–606.
35. Chiang TP, Sheu TWH, Fang CC. Numerical investigation of vortical evolution in a backward-facing step expansion flow. *Applied Mathematical Modeling* 1999; **23**:915–932.
36. Spotz WF. High-order compact finite difference schemes for computational mechanics. *Ph.D. Dissertation*, The University of Texas at Austin, 1995.
37. Barton IE. The entrance effect of laminar flow over a backward-facing step geometry. *International Journal for Numerical Methods in Fluids* 1997; **25**:633–644.
38. Gartling DK. A test problem for outflow boundary conditions-flow over a backward-facing step. *International Journal for Numerical Methods in Fluids* 1990; **11**:953–967.
39. Gresho PM, Gartling DK, Torczynski JR, Cliffe KA, Winters KH, Garratt TG, Spence A, Goodrich JW. Is a steady viscous incompressible two-dimensional flow over a backward-facing step at Re=800 stable? *International Journal for Numerical Methods in Fluids* 1993; **17**:501–541.
40. Ghia U, Ghia KN, Shin CT. High-Resolutions for incompressible flow using the Navier–Stokes equations and a multigrid method. *Journal of Computational Physics* 1982; **48**:387–411.
41. Erturk E, Corke TC, Gokcol C. Numerical solutions of 2-D steady incompressible driven cavity flow at high Reynolds numbers. *International Journal for Numerical Methods in Fluids* 2005; **48**:747–774.
42. Yang JY, Yang SC, Chen YN, Hsu CA. Implicit weighted ENO schemes for the three-dimensional incompressible Navier–Stokes equations. *Journal of Computational Physics* 1998; **146**:464–487.
43. Esfahanian V, Hejranfar K, Mahmoodi Darian H. Implementation of high-order compact finite-difference method to parabolized Navier–Stokes schemes. *International Journal for Numerical Methods in Fluids* 2008; **58**(6):659–685.

DOI: 10.1002/fld